

Predicting Fire Season Intensity in Maritime Southeast Asia with Interpretable Models

William S. Daniels¹, Rebecca R. Buchholz², Helen M. Worden², Fatimah Ahamad³, Dorit M. Hammerling¹

¹Colorado School of Mines, Golden CO, USA

²National Center for Atmospheric Research, Boulder CO, USA

³AQ Expert Solutions, Jalan Dato Muda Linggi, Negeri Sembilan, Malaysia

Corresponding author: William Daniels

Email: wdaniels@mines.edu

Twitter: [@WillSDaniels1](https://twitter.com/WillSDaniels1)

This manuscript has been submitted for publication in JGR: Atmospheres and has not yet undergone formal peer review nor been accepted for publication. Subsequent versions of this manuscript may have slightly different content. If accepted, a final version of this manuscript will be available via the “Peer-reviewed publication DOI” link on the right-hand side of this webpage. Feel free to contact the corresponding author, William Daniels. Feedback is welcome.

1 **Predicting Fire Season Intensity in Maritime Southeast**
2 **Asia with Interpretable Models**

3 **William S. Daniels¹, Rebecca R. Buchholz², Helen M. Worden²,**
4 **Fatimah Ahamad³, Dorit M. Hammerling¹**

5 ¹Colorado School of Mines, Golden CO, USA

6 ²National Center for Atmospheric Research, Boulder CO, USA

7 ³AQ Expert Solutions, Jalan Dato Muda Linggi, Negeri Sembilan, Malaysia

8 **Key Points:**

- 9 • Atmospheric CO variability is connected to climate mode indices through regional
10 fire intensity.
11 • The role of some indices in explaining CO variability changes as their lead time
12 increases.
13 • Our models have good predictive skill at lead times of up to six months in Mar-
14 itime Southeast Asia.

Corresponding author: William Daniels, wdaniels@mines.edu

Abstract

There have been many extreme fire seasons in Maritime Southeast Asia (MSEA) over the last two decades, a trend which will likely continue, if not accelerate, due to climate change. Fires, in turn, are a major driver of atmospheric carbon monoxide (CO) variability, especially in the Southern Hemisphere. Previous studies have explored the relationship between climate variability and fire counts, burned area, and atmospheric CO through regression models that use climate mode indices as predictor variables. Here we model the connections between climate variability and atmospheric CO at a level of complexity not yet studied and make accurate predictions of atmospheric CO (a proxy for fire intensity) at useful lead times. To do this, we develop a regularization-based statistical modeling framework that can accommodate multiple lags of a single climate index, which we show to be an important feature in explaining CO. We use this framework to present advancements over previous modeling efforts, such as the inclusion of outgoing longwave radiation (OLR) anomalies, the use of weekly data, and a stability analysis that adds weight to the scientific interpretation of selected model terms. We find that the El Niño Southern Oscillation (ENSO), the Dipole Mode Index (DMI), and OLR (as a proxy for the Madden-Julian Oscillation) at various lead times are the most significant predictors of atmospheric CO in MSEA. We further show that the model gives accurate predictions of atmospheric CO at lead times of up to 6 months, making it a useful tool for fire season preparedness.

1 Introduction

The relationship between fire and climate has been extensively studied. Fire intensity and burned area are related to the amount, type, and dryness of available fuel, all of which respond closely to water conditions driven by climate variability (van der Werf et al., 2008). This relationship is complex and varies across the different regions of the globe. For instance, drought conditions were found to increase fire potential in Southern Africa, but decrease fire potential in Northern Africa (Andela & van der Werf, 2014).

Climate modes, such as the El Niño Southern Oscillation (ENSO), capture variability in the global climate system. Studies have used these climate modes to help explain the complex relationship between climate and fire, often via regression models. ENSO has been found to influence fires in North America (Mason et al., 2017; Shabbar et al., 2011), Maritime Southeast Asia (Chen et al., 2017; Fuller & Murphy, 2006; Reid et al., 2012), the Amazon (Alencar et al., 2011; Fonseca et al., 2017), and Africa (Andela & van der Werf, 2014; N'Datchoh et al., 2015). Furthermore, studies have found that fire behavior can respond to several distinct climate modes (Andreoli & Kayano, 2006; Chen et al., 2016; Saji & Yamagata, 2003), with Cleverly et al. (2016) showing that the interactions between these climate modes are particularly important for explaining drought and rainfall in Australia (which in turn are major drivers of fire activity). This indicates that fire behavior is affected not only by the isolated influence of multiple modes, but also by their interactions (i.e., whether or not the modes are in phase).

In addition to identifying the climate modes that most influence fire behavior in a given region, studies such as Chen et al. (2016) and Wooster et al. (2012) identify lead times that correspond to the maximum predictive skill of the climate modes being studied. Similarly, Shawki et al. (2017) examines how far in advance the 2015 fire event in Indonesia can be predicted using climate based models, finding that lead times of up to 25 weeks can still provide useful predictions.

These fire-climate connections have been previously studied using satellite observations of fire properties (e.g., Ceccato et al. (2010), Chen et al. (2016), and Wooster et al. (2012)). The Moderate Resolution Imaging Spectroradiometer (MODIS) instruments onboard the Terra and Aqua satellites provide fire count data for each overpass as well

65 as a burned area data product (Giglio et al., 2016, 2018). However, using fire counts or
66 burned area directly presents a number of challenges. Fire counts ignore differences in
67 fire size and intensity, and burned area products potentially miss small fires, underground
68 peat fires, and fires obscured by smoke (although significant improvements in this regard
69 have been made with the most recent product) (Giglio et al., 2018; Shawki et al., 2017).

70 One alternative is to model atmospheric carbon monoxide (CO) instead of fire counts
71 or burned area directly. CO is produced by incomplete combustion from biomass burn-
72 ing, fossil fuel use, and indirectly by photochemistry (Buchholz et al., 2018; Holloway
73 et al., 2000), and its link to fires is well established (Edwards, Emmons, et al., 2006). In
74 fact, biomass burning is the primary source of atmospheric CO variability in the South-
75 ern Hemisphere, making CO anomalies a useful proxy for fire intensity (Bloom et al., 2015;
76 Buchholz et al., 2021; Voulgarakis et al., 2015). As discussed earlier, biomass burning
77 responds to variability in the climate. Since CO variability in the Southern Hemisphere
78 is closely linked to biomass burning, we expect that it also responds to variability in the
79 climate. Compared to the study of fire counts and burned area, less research has gone
80 into the connection between atmospheric CO and climate variability. Furthermore, mod-
81 eling atmospheric CO concentrations provides information on co-emitted atmospheric
82 pollutants in addition to being a proxy for fire intensity.

83 Edwards, Pétron, et al. (2006) found that CO observations from the Measurement
84 of Pollution in the Troposphere (MOPITT) instrument are correlated with ENSO. Buchholz
85 et al. (2018) expanded on Edwards, Pétron, et al. (2006), finding that atmospheric CO
86 anomalies in a number of Southern Hemisphere regions are related to four different cli-
87 mate modes (including ENSO) and that the interactions between these climate modes
88 are important for explaining atmospheric CO anomalies. In this study, we also exam-
89 ine the relationship between atmospheric CO and climate variability, further focusing
90 on the Maritime Southeast Asia (MSEA) region because of its extremely large CO anoma-
91 lies (Buchholz et al., 2021). While we focus on a single region in this paper, the mod-
92 eling framework we have developed can easily be applied to other parts of the globe.

93 We extend the models from Buchholz et al. (2018) via the following advancements.
94 First, we use week-averaged data rather than month-averaged data, significantly increas-
95 ing predictive skill. Second, we include the Madden-Julian Oscillation (MJO) via a proxy
96 index, resulting in models that are better able to capture extreme CO anomalies in MSEA.
97 Third, we develop a regularization-based model fitting framework that allows for mod-
98 els with multiple lags of a single climate mode. Fourth, we assess the stability of the se-
99 lected model terms, which adds weight to their scientific interpretation and increases over-
100 all model interpretability. Finally, we make it possible to set the desired lead time of model
101 predictions, better gearing models towards practical use in fire season intensity forecast-
102 ing. These advancements result in models that extend those presented in Buchholz et
103 al. (2018) by capturing more complex relationships and having better predictive perfor-
104 mance while remaining human-interpretable. As a result, we believe that these models
105 better explain the climate-atmospheric chemistry connections in MSEA and can serve
106 as useful tools for fire season preparedness.

107 The rest of this paper is laid out as follows. In Sections 2 and 3, we describe the
108 data and our statistical model, respectively. In Section 4, we discuss our model fitting
109 framework. In Sections 5 and 6, we present results and assess improvements in model
110 interpretability and predictive skill, respectively, over the models presented in Buchholz
111 et al. (2018). Finally, we summarize our work in Section 7.

112 2 Observational Data Sets

113 We model atmospheric CO using a linear regression framework in which the response
114 variable (CO) is modeled as a linear combination of predictor variables (climate mode

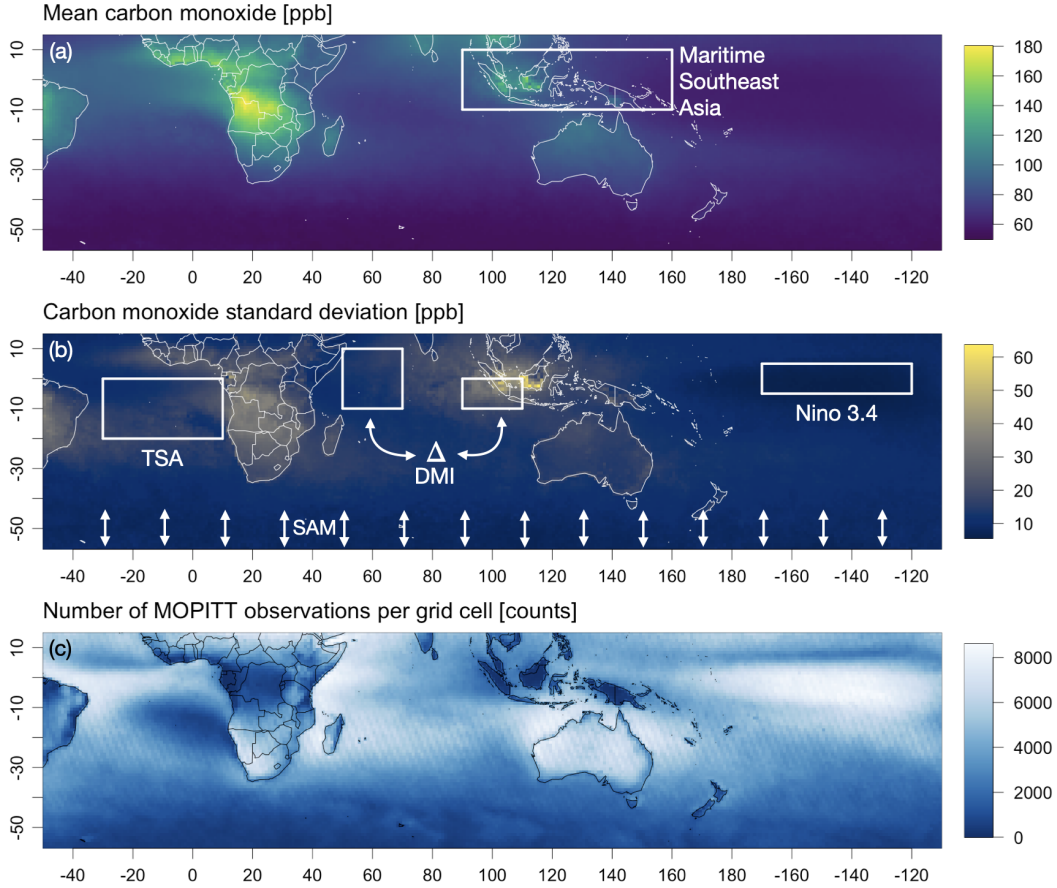


Figure 1. MOPITT CO data during the Southern Hemisphere fire season (defined here as September through December) from 2001 to 2019. Data are filtered as described in Section 2.1. (a) Average of all MOPITT CO observations ($n = 217,995,648$) with the Maritime Southeast Asia (MSEA) region shown in white. (b) CO standard deviation with the spatial range of influence of the four climate mode indices discussed in Section 2.2 shown in white. (c) Number of MOPITT observations falling within each grid cell. Note that the landmasses in MSEA have fewer observations than other regions, which could be influencing the high CO standard deviations in this region. All three subfigures are plotted on the same $1^\circ \times 1^\circ$ grid.

115 indices and their proxies). The following subsections describe the data used as our re-
 116 sponse and predictor variables.

117 **2.1 Response Variable**

118 For the response, we use carbon monoxide column-averaged volume mixing ratios
 119 (referred to as simply CO) from the MOPITT instrument onboard the Terra satellite
 120 (Drummond et al., 2010). The units of column-averaged volume mixing ratios are parts
 121 per billion by volume (ppb). Using column-averaged volume mixing ratios instead of total
 122 column CO removes dependence on surface topography and pressure changes (Buchholz
 123 et al., 2021).

124 MOPITT has complete Earth coverage about every three days with a footprint size
 125 of $22 \times 22 \text{ km}^2$. We use the V8 retrieval algorithm with validation results described in

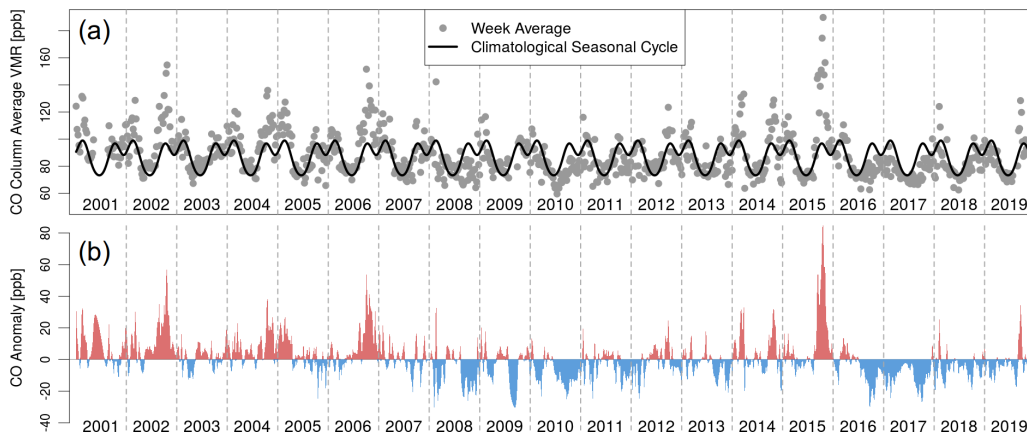


Figure 2. (a) Weekly CO observations for the MSEA region (grey circles) and the climatological average created by averaging each week over the 19-year time series (black line). (b) CO anomalies resulting from the difference between the weekly observations and the climatological average. Positive anomalies are shown in red and negative anomalies are shown in blue.

126 Deeter et al. (2019). To reduce systematic and random error, we select daytime, land-
 127 only retrievals from the joint near infrared (NIR) and thermal infrared (TIR) product.
 128 Daytime retrievals over land have a higher sensitivity to CO than nighttime or ocean re-
 129 trievals due to higher thermal contrast. We use the joint product because it includes ad-
 130 ditional information from reflected solar radiation over land (Worden et al., 2010). See
 131 Buchholz et al. (2018), Deeter et al. (2007), and Deeter et al. (2014) for details.

132 We aggregate CO observations into a single biomass burning region in the South-
 133 ern Hemisphere: Maritime Southeast Asia (MSEA). We focus on MSEA because it is a
 134 biomass burning region that experiences significant CO anomalies (i.e., concentrations
 135 well above average) (Buchholz et al., 2021). Note that this methodology has been ap-
 136 plied to other regions as well (including Southeast Australia - the region that experienced
 137 severe bushfires in 2019 and 2020), but for brevity, we discuss only results from MSEA
 138 in this paper. Figure 1(a) shows the MSEA region.

139 We create a weekly time series for MSEA by averaging all of the observations falling
 140 within the region boundaries for each week. This time series ranges from 2001 to 2019,
 141 resulting in 19 years of data and 991 weekly observations. We compute the seasonal cy-
 142 cle by taking an average over the 19 years of data for each week. We then remove this
 143 seasonal cycle from the weekly time series so that our models are better able to capture
 144 the anomalous CO observations corresponding to large burn events. Figure 2 shows the
 145 weekly CO observations, climatological average, and resulting anomalies for the MSEA
 146 region.

147 Finally, since we are interested in using CO as a proxy for fires, we only model anoma-
 148 lies during the fire season in the Southern Hemisphere, defined here as September through
 149 December. This time frame was selected based on results from Buchholz et al. (2018)
 150 which showed that these months captured most of the atmospheric CO variability in the
 151 MSEA region. Specifying the time frame in this way results in a total of 330 weekly ob-
 152 servations.

153 2.2 Predictor Variables

154 We are interested in connections between atmospheric CO and climate variability.
 155 Climate modes are large scale patterns that capture variation in temperature, wind, or

156 other aspects of climate over certain spatial regions. A well known example is ENSO,
 157 which captures quasi-periodic variability in sea surface temperature and wind in the Pa-
 158 cific Ocean (Neelin et al., 1998; Trenberth, 2013). Climate indices are metrics that quan-
 159 tify the state of climate modes.

160 As in Buchholz et al. (2018), we consider four climate modes that represent vari-
 161 ability in the major ocean basins of the Southern Hemisphere and tropics. The ENSO
 162 represents the Pacific Ocean, the Indian Ocean Dipole (IOD) represents the Indian Ocean,
 163 the Tropical South Atlantic (TSA) represents the southern Atlantic Ocean, and the Antarc-
 164 tic Oscillation (AAO) represents the Southern Ocean.

165 For predictor variables, we select a single climate mode index to represent each of
 166 these climate modes. To represent the ENSO, we use the Niño 3.4 index defined in Bamston
 167 et al. (1997). To represent the TSA, we use the Tropical South Atlantic Index defined
 168 in Enfield et al. (1999). These two indices are calculated using sea surface temperature
 169 (SST) anomalies in the regions shown in Figure 1(b) labeled as Niño 3.4 and TSA, re-
 170 spectively. To represent the IOD, we use the Dipole Mode Index (DMI) defined in Saji
 171 et al. (1999). This index is calculated from SST gradients between the two regions shown
 172 in Figure 1(b) labeled as DMI. To represent the AAO, we use the Southern Annular Mode
 173 (SAM) index defined in Thompson and Wallace (2000). This index captures Antarctic
 174 atmospheric circulation described by the poleward shift of westerly winds. This index
 175 is calculated by projecting observational height anomalies at 700 hPa and poleward of
 176 -20 degrees latitude onto the leading empirical orthogonal function of the National Cen-
 177 ters for Environmental Prediction and National Center for Atmospheric Research reanal-
 178 ysis (Kalnay et al., 1996; Kistler et al., 2001). The spatial extent of this index is shown
 179 in Figure 1(b) via the arrows labeled SAM. We expect a relationship between these in-
 180 dices and CO, as each index is related to regional climate (e.g., rainfall), which in turn
 181 affects drought, fire, and ultimately CO concentrations.

182 In addition to these four indices, we also want to include variability captured by
 183 the MJO in our models. This climate mode broadly describes the eastward propagation
 184 of a convection cell that forms off the east coast of Africa and dissipates in the Pacific Ocean
 185 (Madden & Julian, 1972). The MJO is the dominant mode of intraseasonal variability
 186 in the tropics (Madden & Julian, 1994) and has been shown to increase or decrease the
 187 probability of extreme rain events by over 20% in the MSEA region depending on its phase
 188 (Xavier et al., 2014). The most common MJO index is described by the two primary em-
 189 pirical orthogonal functions (EOFs) resulting from a number of climate variables (Wheeler
 190 & Hendon, 2004). However, this index is not well suited for a regression framework, as
 191 it would require a main term for both EOFs and their interaction to properly capture
 192 the phase of the MJO. This introduces multiple coefficient estimates for a single phys-
 193 ical phenomenon, which makes it harder to model and hinders model interpretability.

194 Instead of using these EOFs, we use outgoing longwave radiation (OLR) anom-
 195 alies to capture variability described by the MJO in our models. OLR is a metric that
 196 describes how much energy is leaving the atmosphere and is one climate variable used
 197 in Wheeler and Hendon (2004) to produce the EOF index. Low OLR values indicate the
 198 presence of clouds, and hence a higher likelihood of rainfall (Birch et al., 2016). There-
 199 fore, using OLR anomalies in the MSEA region as a proxy for the MJO provides a sin-
 200 gle metric that captures the presence of the convection cell described by the MJO. This
 201 proxy is better suited for a regression analysis despite losing some of the information con-
 202 tained in the EOF index from Wheeler and Hendon (2004).

203 We aggregate OLR values over the same spatial region that defines the MSEA re-
 204 gion shown in Figure 1, and we create anomalies in the same manner as the CO anom-
 205 alies described in Section 2.1. We demonstrate the benefit of including the OLR proxy
 206 in Section 6.1.



Figure 3. Time series of the five climate mode indices used as predictor variables in this study. Note that OLR is used as a proxy index for the MJO and that DMI is plotted using a different vertical scale.

207 Figure 3 shows the weekly time series for each climate mode index used as a pre-
 208 dictor variable in this study. Some of the indices have both high and low frequency
 209 components. This is most obvious in the SAM and OLR. We believe that the high frequency
 210 component of the OLR captures the oscillatory movement of the convection cell described
 211 by the MJO because both have a period of around 30 to 90 days. The climate mode in-
 212 dex data used in this study are publicly available. The source of each index (or proxy
 213 index in the case of the MJO) is listed in Table 1.

Table 1. Climate mode indices used in this study with links to their sources. Note that we use OLR as a proxy index for the MJO.

Climate Mode	Metric Used in Model	Source
ENSO	Niño 3.4	NOAA OOPC (2021)
IOD	Dipole Mode Index (DMI)	NOAA OOPC (2021)
TSA	Tropical South Atlantic (TSA)	NOAA OOPC (2021)
AAO	Southern Annular Mode (SAM)	NOAA CPC (2021)
MJO	Outgoing Longwave Radiation (OLR)	NOAA PSL (2021)

3 Multiple Linear Regression Model

214 We use lagged multiple linear regression to model the relationship between CO anoma-
 215 lies and climate mode indices. We include first order interaction terms to capture the
 216 interconnected nature of the global climate system. Buchholz et al. (2018) found that
 217 these interaction terms were highly significant in explaining CO variability. Unlike the
 218 models in Buchholz et al. (2018), we also include squared terms to capture potential non-
 219 linear relationships between the mean CO response and the climate mode indices. For
 220 a given region, we assume that
 221

$$CO(t) = \mu + \sum_k a_k \chi_k(t - \tau_k) + \sum_{i,j} b_{ij} \chi_i(t - \tau_i) \chi_j(t - \tau_j) + \sum_l c_l \chi_l(t - \tau_l)^2 + \epsilon(t), \quad (1)$$

where $CO(t)$ is the CO anomaly at time t , μ is a constant mean displacement, a_k , b_{ij} , and c_l are coefficients, χ are the climate indices, τ is the lag value for each index in weeks, $\epsilon(t)$ is a random error component, and k, i , and j iterate over the number of climate indices used in the analysis. Note that we standardize the climate indices, χ , before fitting the model so that coefficient estimates can be directly compared. We consider lags between one and 52 weeks for each index, excluding zero week lags so that our models can be used for prediction. We also enforce strong hierarchy, meaning that any covariate that appears in an interaction or squared term must also appear as a main effect. Strong hierarchy has long been recommended for models with interactions, as it helps avoid misinterpretation of the included covariates (Nelder, 1977). See the Supporting Information file for more details on strong hierarchy.

Although the high frequency variability present in the weekly climate index data has important near-term effects, we do not expect it to have a large impact on the amount, type, and dryness of available fuel far into the future. This is because we believe that short anomalies do not last long enough to drastically alter large scale fuel reserves. Therefore, we want covariates with longer lags to capture progressively lower frequency components of the climate indices.

To accomplish this, we apply more smoothing to the climate mode indices as the length of their lag in the statistical model increases. In brief, we do not smooth indices for lags below four weeks to capture as much high frequency signal as possible in these short term relationships. For lags between four and 52 weeks, we use Gaussian kernels to linearly increase the amount of smoothing applied to the indices. More information on our smoothing scheme can be found in the Supporting Information file.

4 Variable Selection and Model Fitting

We consider 52 lags of each climate mode index, quadratic terms, and all pairwise interactions, which results in far more covariates than observations. In this regime, there is not a unique least squares solution, so another model fitting method is needed to compute coefficient estimates. Furthermore, we want to perform variable and lag selection to obtain human-interpretable models. Buchholz et al. (2018) broke this process up into two parts. First, they iterated through all possible lag combinations. At a given combination of lag values, stepwise selection was used for variable selection. This resulted in a list of optimally performing models, with one model for each combination of lag values. Adjusted R^2 was then used to select a single model from this list. By iterating through the lag values in this manner, Buchholz et al. (2018) was able to use stepwise selection without large computational resources. However, this strategy allowed for only a single lag of each index in the models.

To capture more complex relationships involving multiple lags of a given index, we instead consider all possible lags for each index simultaneously. This makes the search space too large for stepwise selection, so we instead employ regularization for both variable and lag selection. In the linear regression setting, regularization is a method of computing coefficient estimates that balances model fit and the overall magnitude of the coefficients with the goal of finding models that generalize well to new data. Furthermore, regularization is well suited for problems with more covariates than observations, making it feasible to consider all lag values for each index simultaneously.

We use a flexible regularization penalty called the Minimax Concave Penalty (MCP) (Zhang, 2010). Similar to the Least Absolute Shrinkage and Selection Operator (LASSO)

penalty (Tibshirani, 1996), the MCP shrinks insignificant coefficient estimates to exactly zero, which leads to interpretable models with relatively few terms. Additionally, the MCP results in less biased estimates for the remaining non-zero coefficients by allowing for larger coefficients on the significant terms (Zhang, 2010). We found that using the MCP instead of the LASSO increased model performance. The MCP introduces a second parameter, η , that controls the MCP penalty in addition to the tuning parameter, λ , which is present in all regularization methods. The λ parameter balances how well the model fits to data and the overall magnitude of the coefficients (with a smaller overall magnitude leading to models with less terms). Compared to the LASSO, the MCP relaxes as the coefficients get larger and plateaus after they reach a certain magnitude. The η parameter controls when this plateau occurs, with smaller η values enabling larger coefficient estimates on the significant terms. Optimal λ and η values need to be learned from data.

To select parameter values, we perform a simple grid search over a range of η and λ values. We use the MCP to fit a model at each combination of η and λ values (implemented in R via the RAMP package from Hao et al. (2018)). We then choose between the resulting models via the Extended Bayesian Information Criterion (EBIC). The EBIC applies a much stronger penalty to large models (i.e., models with many selected terms) than other information criteria through a third parameter, γ , which is defined on the range $[0, 1]$. When $\gamma = 0$, the EBIC is identical to the Bayesian Information Criterion (BIC), but when $\gamma = 1$, the EBIC is much harsher than the BIC. This is well suited for applications in which the number of possible covariates is large, but the optimal model might in fact be quite small. Since the number of potential covariates in this application is vast (recall that each lag value represents a different covariate), we use the EBIC rather than the BIC to select the final model. After finalizing the model terms in this manner, we refit their coefficient estimates via maximum likelihood.

More details on regularization, the MCP, the EBIC, and how we select parameter values can be found in the Supporting Information file. In the remaining sections, we discuss how this modeling framework and the choice of γ can be used to address our two goals of model interpretability and predictive skill.

5 Interpreting Fitted Models

Here we examine the physical implications of the models fit using the procedure described in Section 4. We focus on connections between climate and atmospheric chemistry in MSEA through an analysis of selected indices and lag values.

5.1 A Framework for Identifying Optimally Performing Models at Various Complexities

We can create a list of “optimally performing” models at decreasing complexities (i.e., number of terms) by increasing the EBIC parameter, γ , on the range $[0, 1]$, as larger γ values increase the penalty on large models. Optimal here refers to the fact that these models are the result of a grid search over the other two free parameters, λ and η . For the MSEA region, this procedure results in the models listed in Figure 4. The color of each box corresponds to the γ value that was used to generate the model contained within it. Note that multiple γ values can produce the same models. Within each box, the name of the index and the corresponding lag is listed (in the format “name_lag”), along with the coefficient estimates and standard errors.

Moving from left to right in Figure 4, we see that the models decrease in size (from 17 terms to nine), while their performance drops only slightly (from explaining 70% of variability in the response to 61%). By examining the terms that remain in the model

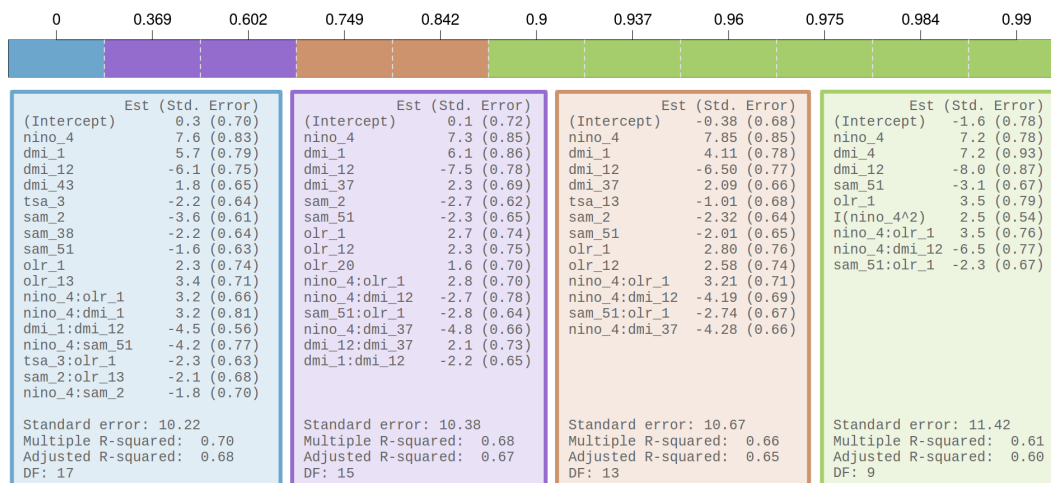


Figure 4. Optimal models for the MSEA region for a logarithmic sequence of γ values. Note that multiple γ values can produce the same model. The color of each box corresponds to the γ value that was used to generate the model contained within it. Within each box, the selected model terms are listed in the format “name_lag,” where lags are in weeks. Coefficient estimates and standard errors are listed for each term, and summary statistics are listed below each model. Note that “nino” refers to the Niño 3.4 index.

317 as it becomes more parsimonious, we can determine which indices and lags are most in-
 318 influential in explaining variability in the response.

319 For the MSEA region, we can see that the Niño 3.4 index lagged at four weeks re-
 320 mains in the model with a positive coefficient estimate. This makes sense, as ENSO is
 321 a major climate driver in the tropics, with positive anomalies resulting in warmer, drier
 322 conditions (Nur’utami & Hidayat, 2016). The lag of four weeks indicates that it takes
 323 about four weeks for the effect of a Niño 3.4 anomaly to impact CO anomalies. Addi-
 324 tionally, the Niño 3.4 lag of four weeks appears as a squared term in the most parsimo-
 325 nious model, indicating that there is a nonlinear relationship between Niño 3.4 and CO.
 326 This is confirmed by examining the residuals of a model fit to solely the Niño 3.4 lag of
 327 four weeks (not shown).

328 The selected DMI lags also suggest an interesting relationship. Note that positive
 329 DMI anomalies are associated with reduced rainfall in parts of MSEA, while negative
 330 DMI anomalies are associated with increased rainfall (Nur’utami & Hidayat, 2016). A
 331 DMI lag of 12 weeks remains in the model as it become more parsimonious, as well as
 332 a shorter lag that switches from one to four weeks between the smallest two models. The
 333 coefficient on the longer lag is negative, while the coefficient on the shorter lag is pos-
 334 itive. The coefficient on the shorter lag implies that reduced rainfall (i.e., positive DMI
 335 anomalies) results in more CO on average, and vice versa. This is likely the result of an
 336 intuitive relationship: reduced rainfall leads to drier conditions that are more prone to
 337 burning (and hence more CO). Similar to the ENSO relationship, these dry conditions
 338 take one to four weeks to impact CO. The coefficient on the longer lag, however, implies
 339 the opposite: reduced rainfall (i.e., positive DMI anomalies) results in less CO on aver-
 340 age, and conversely, increased rainfall results in more CO on average. This could be be-
 341 cause rainfall leads to vegetation growth, which ultimately provides more fuel for fires.
 342 The length of this lag is longer, implying that it takes around 12 weeks for the increased
 343 vegetation growth to impact CO concentrations.

344 The effect of these two DMI lags is compounding. That is, more vegetation as a
 345 result of DMI-driven rainfall at a 12 month lag leads to more fuel when a subsequent pos-
 346 itive DMI anomaly creates dry conditions. This is supported by the negative coefficient
 347 on the interaction between the DMI lag of 12 weeks and one week present in the largest
 348 model in Figure 4. Because the coefficient is negative, there is less CO on average when
 349 the DMI has the same phase (i.e., either a positive or negative anomaly) at both a 12
 350 and one week lag.

351 An OLR term lagged at one week remains in the MSEA model as it becomes more
 352 parsimonious with a positive coefficient estimate. This again makes sense, as positive OLR
 353 anomalies are associated with less cloud cover and hence less rain. The one week lag sug-
 354 gests that an OLR-driven decrease in rain leads to more CO in the short term, likely as
 355 a result of increased burning. The TSA index, on the other hand, is only included in the
 356 largest model. This could be because the TSA describes sea surface temperatures in the
 357 southern Atlantic Ocean, which is very far from the MSEA region. Therefore, it makes
 358 sense that the TSA is less important than the other indices in explaining CO variabil-
 359 ity in MSEA, as the other indices are based on aspects of the global climate system lo-
 360 cated closer to MSEA.

361 Finally, two Niño 3.4 interaction terms remain in the model as it becomes more par-
 362 simonious. One interaction is with the OLR at a one week lag and the other is with the
 363 DMI at a 12 week lag. The sign of these interaction terms is the same as the non-Niño
 364 3.4 component. This indicates that the effects of these indices are amplified when they
 365 are in phase, a result that has been previously identified in the literature (Cleverly et
 366 al., 2016; Nur’utami & Hidayat, 2016).

367 Note that these findings largely agree and expand upon the results in Buchholz et
 368 al. (2018). For the MSEA region, Buchholz et al. (2018) found that a Niño 3.4 lag of one
 369 month, DMI lag of eight months, TSA lag of five months, and SAM lag of one month
 370 were important predictors. The largest model presented in this study contains a Niño
 371 3.4 lag of four weeks, DMI lag of 43 weeks, TSA lag of three weeks, and SAM lag of two
 372 weeks. All but the TSA term (which we will show to be less important for the MSEA
 373 region in Section 5.2) agree closely on their selected lag. However, the models we present
 374 here are capable of including multiple lags of a single index, which expands on the work
 375 in Buchholz et al. (2018) and highlights more complex relationships between climate and
 376 CO.

377 5.2 Assessing Stability of Selected Model Terms

378 While the scientific conclusions drawn in the previous section seem to broadly agree
 379 with the literature, we want to ensure that the selected covariates are in fact meaning-
 380 ful. That is, we want to avoid over-interpreting the role of covariates if slight changes
 381 in data result in drastically different models, as these models would not be capturing a
 382 meaningful physically-based relationship but would rather be artifacts of the specific train-
 383 ing data.

384 Therefore, we perform one-year-out resampling to assess the stability of selected
 385 covariates. We perform the resampling on the largest model from Figure 4 because it con-
 386 tains most of the terms present in the smaller models. Specifically, we perform the fol-
 387 lowing resampling procedure. We first iterate through the years present in the data. For
 388 each year, we create a testing set containing all data falling within that year and a train-
 389 ing set containing the remainder of the data. We then train two models using only data
 390 from the training set. We force the first model (called the “main model”) to retain the
 391 same covariates as the model trained on all of the data but allow for different coefficient
 392 estimates. We let the second model (called the “new model”) to completely change based
 393 on the particular training set, meaning that it can have different covariates and coeffi-
 394 cient estimates than the model trained on all of the data. We then test these two mod-

395
396

els on the corresponding test set and compute the root mean square error (RMSE) for both.

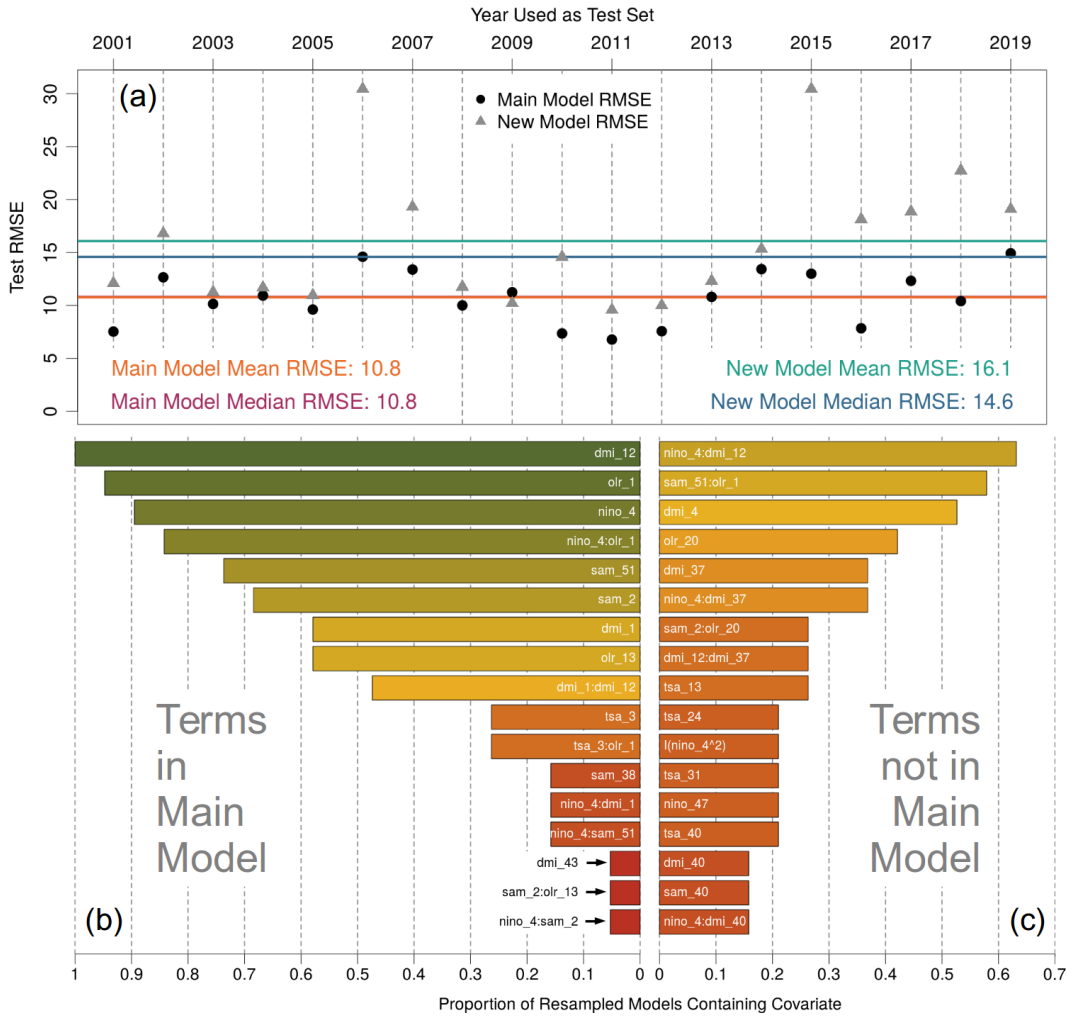


Figure 5. Results from the one-year-out resampling. Main model refers to the model forced to retain the structure of the model trained on all of the data, but with refit coefficient estimates. New model refers to the model allowed to completely change according to the particular training set. (a) shows the out-of-sample prediction error for each training set. The year on the horizontal axis indicates which year was used to test the models. The main model almost always outperforms the new model. (b) shows the frequency with which main model terms appear in the new models. Similarly (c) shows the frequency with which terms not present in the main model appear in the new model. The most significant covariates from Figure 4 appear in many of the retrained models. The color in (b) and (c) corresponds to the proportion on the horizontal axis and is included for visual clarity. Note that “nino” refers to the Niño 3.4 index.

397
398
399
400
401

Figure 5 shows the results of this resampling and is divided into three sections. Figure 5(a) shows the out-of-sample prediction error (RMSE) from both models for each different training set. The year on the horizontal axis corresponds to the year reserved for the testing set. The RMSE of the main model (that is, the model that retains the structure of the model trained on all data) tends to perform as well or better than the

402 model allowed to completely change according to the new training set. This provides jus-
 403 tification for using the form of the main model as the representative model for the MSEA
 404 region and further interpreting its covariates, as the relationships captured by this model
 405 do a better job at explaining the data than those in the new models. Note that the RMSE
 406 of the new model is significantly larger when 2006 and 2015 are left out of the training
 407 set. These years have some of the largest CO anomalies (see Figure 2), which indicates
 408 that these extreme years are important in driving the form of the model.

409 Figure 5(b) and Figure 5(c) show how often certain terms appear in the new mod-
 410 els (that is, the models allowed to completely change according to the new training data).
 411 This gives some indication of the stability of the various model terms. If a term is present
 412 in many of the retrained models, then the modeling framework is likely picking up a physically-
 413 based relationship. Terms that are absent from many of the retrained models are more
 414 likely artifacts of the specific training set, rather than a true physical relationship.

415 Figure 5(b) shows how often the main model terms reappear in the new models.
 416 Notably, the terms present in the most parsimonious model from Figure 4 are most likely
 417 to appear in the retrained models. This indicates that these terms are explaining the most
 418 stable aspect of the physical relationship. Other terms, such as the 43 week DMI lag,
 419 rarely appear in the retrained models. This indicates that less consideration should be
 420 given to these terms when attempting to explain the physical relationship between cli-
 421 mate and CO.

422 Figure 5(c) shows how often terms not present in the main model appear in the
 423 retrained models. Note the different scales on the horizontal axis between subfigures 5(b)
 424 and 5(c). In Figure 5(c) we see that a selection of terms not in the main model appear
 425 relatively frequently in the retrained models. Recall that when moving from the second
 426 smallest to the smallest model in Figure 4, the shorter DMI lag switches from one week
 427 to four weeks. In Figure 5, we see that both the one and four week DMI lags show up
 428 in about half of the retrained models. This indicates that these terms are interchange-
 429 able, and determining which is included likely depends on the other selected covariates.

430 Figures 5(b) and (c) further confirm that the terms present in the most parsimo-
 431 nious model for the region (see Figure 4) are capturing meaningful signal and are not
 432 simply artifacts of the specific training set. This is because these terms remain in a large
 433 majority of the retrained models, each of which is trained on a different subsample of
 434 the data. Furthermore, Figure 5(c) illustrates that the interaction between Niño 3.4 lagged
 435 at four weeks and DMI lagged at 12 weeks, although not present in the main model, is
 436 still a significant interaction in explaining CO variability in MSEA. This also holds for
 437 the interaction between SAM lagged at 51 weeks and OLR lagged at one week. The terms
 438 that are included less often in the retrained models are likely more data dependent and
 439 help the model capture subtleties in the response. As a result, it is more likely that these
 440 terms would change with small changes in the data. An example is the TSA term lagged
 441 at three weeks present in the main model. This term appears in less than 30% of the re-
 442 trained models, which confirms the analysis in Section 5.1 that finds that TSA is less im-
 443 portant in explaining CO variability in MSEA.

444 The stability analysis presented here provides further justification for assigning sci-
 445 entific weight to selected model terms, as it shows that certain stable terms are not sim-
 446 ply artifacts of the particular training set used to fit the model. In particular, we con-
 447 firm that a number of terms from the smallest model presented in Figure 4 are very sta-
 448 ble: DMI lagged at 12 weeks, OLR lagged at one week, Niño 3.4 lagged at four weeks,
 449 a short DMI lag (of either one or four weeks depending on the remaining model terms),
 450 SAM lagged at 51 weeks, the interaction between Niño 3.4 lagged at four weeks and OLR
 451 lagged at one week, and the interaction between Niño 3.4 lagged at four weeks and DMI
 452 lagged at 12 weeks. This provides further evidence that these terms specify the most sig-
 453 nificant relationships between climate and atmospheric CO in MSEA.

6 Assessing Model Predictions

We now turn our attention to the predictive skill of selected models. We again focus on the largest model from Figure 4, as this model has the best predictive capabilities. There is value in making accurate forecasts, as advanced warning of intense fire seasons would give governments enough time to properly staff fire departments, stock up on masks, and warn citizens in high risk areas.

6.1 Model Predictions with No Minimum-Lag-Threshold

In this subsection we impose no requirements on the minimum lag value allowed in the models, meaning that we allow lags of one to 52 weeks as in Figure 4. In Figures 6 and 7 we demonstrate the predictive capabilities of our model and highlight two interesting results.

Figure 6 shows weekly observations and predictions from two model variants. Note that these predictions are in-sample, meaning that they are predictions of the observations used to train the model. The top plot of Figure 6(a) shows predictions from a model completely refit to a data set excluding the OLR, and the bottom plot shows predictions from the full model (i.e., the model presented in Figure 4). We can see that including the OLR results in a slight decrease in RMSE and increase in both R^2 and adjusted R^2 . Note that adjusted R^2 is a better metric for comparing the two models, as it accounts for the number of terms in each model. Similar to R^2 , higher adjusted R^2 values indicate a better fit. Furthermore, in Figure 6(b) and (c), we highlight two of the most anomalous years, which shows that the OLR helps capture the extreme CO anomalies. This makes sense for 2015 in particular, as the MJO and our OLR proxy experienced an extreme anomaly during this year.

Figure 7 shows month-averaged observations and predictions from two different model variants. The top plot of Figure 7(a) shows predictions from a month-based model. To create this model, we took month-averages of the predictor variables and then trained the model on only these month-averaged covariates using the framework presented in Section 4. The bottom plot shows month-averaged predictions from the model trained on weekly data (i.e., the model shown in Figure 4). We see a noticeable increase in model performance when using the weekly data, suggesting that the weekly data is able to capture meaningful signal beyond the month-averages. This is an interesting result, as it suggests that the higher frequency signals present in the climate indices are in fact meaningful signal and not simply noise. This is perhaps most important for OLR (the proxy for localized MJO), which has a higher frequency component than the other included climate indices. This increase in performance can be seen clearly during the 2015 CO anomaly.

Note that the predictions from these models are an improvement over the models in Buchholz et al. (2018). When using week-averaged data to train the model, we are able to explain 87% of the variability in the month-averaged CO observations. The model in Buchholz et al. (2018) explains 75% of the month-averaged CO. This increase in predictive skill is likely a result of: 1) the ability to include multiple lags of a single climate mode index, 2) the additional signal contained in the week-averaged data, and 3) the inclusion of the OLR proxy index.

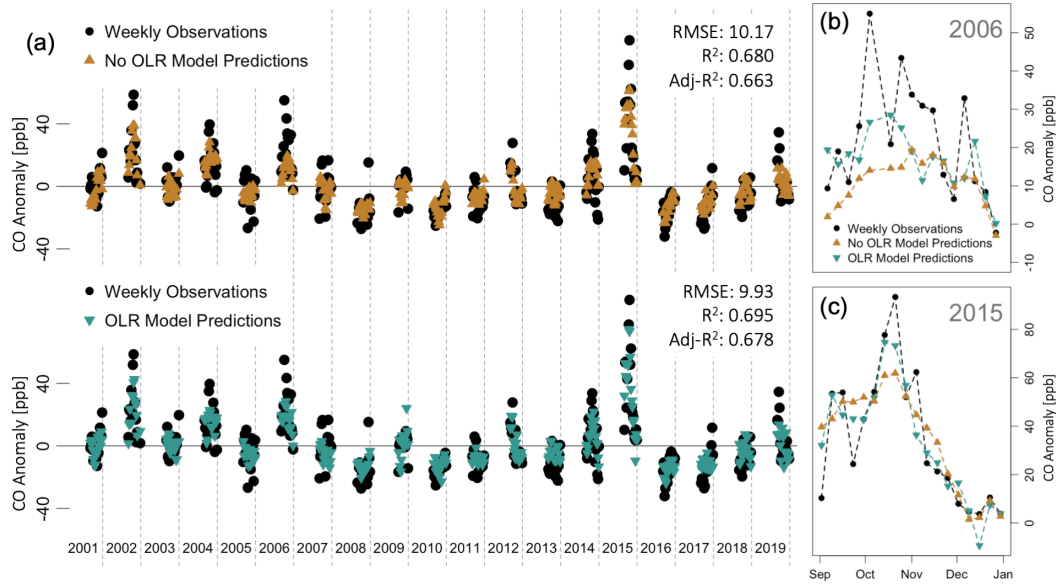


Figure 6. In-sample predictions from two model variants. In (a), the top plot shows predictions from the optimal model without the OLR, and the bottom plot shows predictions from the optimal model with the OLR. Adding the OLR appears to increase predictive skill during the extreme CO anomalies shown in (b) and (c).

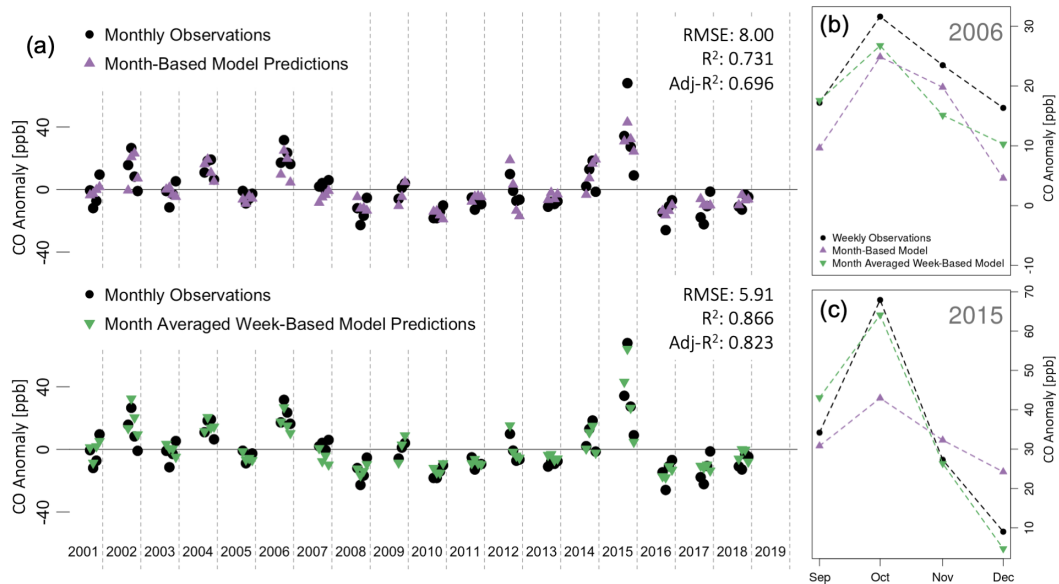


Figure 7. In-sample predictions from two additional model variants. In (a), the top plot shows predictions from a model trained on month-averaged covariates, and the bottom plot shows month-averaged predictions from a model trained on week-averaged covariates. The increase in model performance indicates that there is meaningful signal in the higher frequency climate index data, which is clearly seen in the anomalous years shown in (b) and (c).

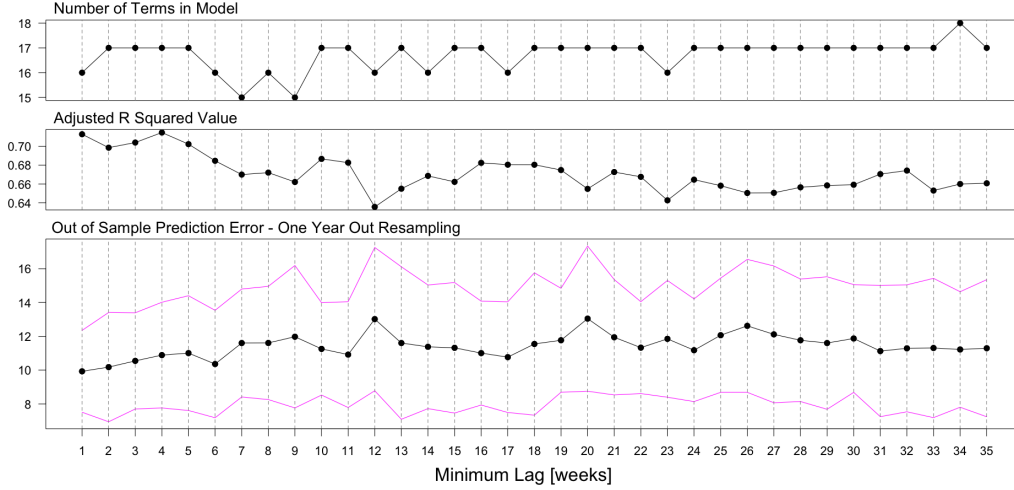


Figure 8. Model performance for the MSEA region at increasing minimum-lag-thresholds. Top plot shows the number of terms in the selected model. Middle plot shows the adjusted R^2 value of the selected model. Bottom plot shows an average out-of-sample prediction error for each model with magenta lines showing \pm one standard deviation. Here we iteratively leave one year out, train the model on the remaining data, and test it on the left out year. Plotted is the average RMSE with \pm one standard deviation lines in magenta from this procedure as a function of minimum lag. We can see that model performance drops off with an increasing minimum-lag-threshold, although at a fairly gradual pace.

496

6.2 Increasing Minimum-Lag-Threshold

497

498

499

500

501

502

The predictions shown in Subsection 6.1 are useful for demonstrating model performance and the comparative benefit of using the OLR and week-averaged data. However, these models include an OLR term lagged at one week (see Figure 4), which significantly reduces their practical utility. This model can only predict as far in advance as the length of its shortest lag, or in this case, one week. Predictions with longer lead times would give governments more time to prepare for intense fire seasons.

503

504

505

506

507

508

509

To increase the prediction horizon, we implement a minimum-lag-threshold that only allows lags greater than the threshold value to be included in the model. Because increasing this threshold reduces the number of possible covariates, we also extend the maximum lag value as the minimum-lag-threshold is increased. Specifically, we consider lags between the minimum-lag-threshold and 52 weeks plus this threshold. This ensures that all models are based on one year of climate data, making it easier to compare their predictive skill.

510

511

512

513

514

515

516

517

518

519

520

Figure 8 shows a selection of model performance metrics as this minimum-lag-threshold is increased. We again focus on the largest model generated from the range of EBIC γ values, as this model has the best predictive skill. The top plot in Figure 8 shows the number of terms in the selected model for each minimum-lag-threshold. The second plot shows the adjusted R^2 value of the selected models. As expected, the model performance drops off as the minimum lag is increased. However, this decline is not very rapid. That is, models with a high minimum-lag-threshold still explain a large percent of the variability in atmospheric CO anomalies. This is promising, as it means that predictions can be made farther in advance without losing too much predictive skill. The third plot shows another performance metric: the average out-of-sample prediction error from one-year-out resampling. Here we successively leave one year out, train the model on the remain-

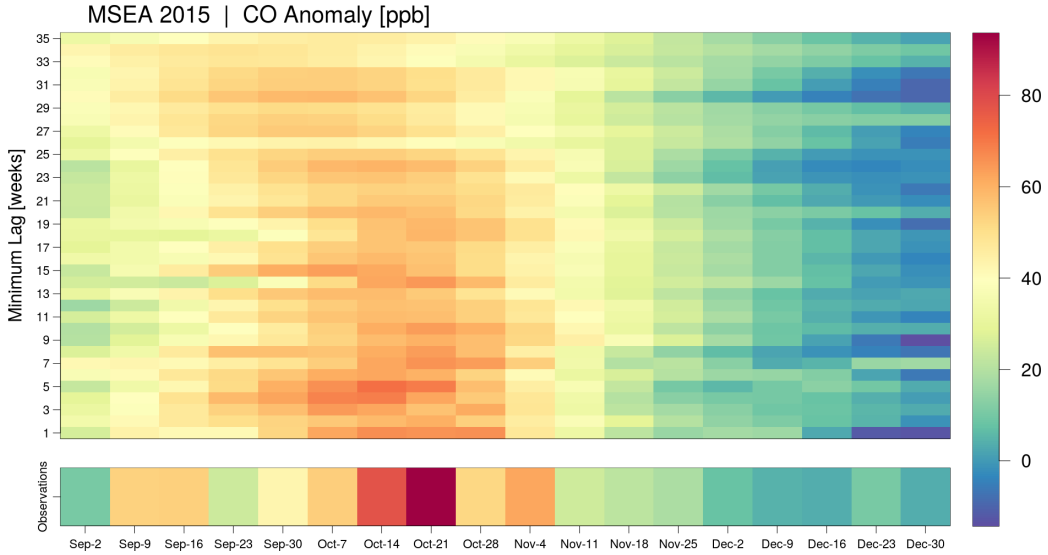


Figure 9. Predictions of the 2015 CO anomalies in the MSEA region for a range of minimum-lag-thresholds. Color represents CO anomalies, and the horizontal axis represents time. MOPITT observations are shown as a horizontal bar along the bottom of the figure. The remaining vertical axis corresponds to the minimum-lag-threshold used to fit the model, and hence each row of the figure contains predictions from a different model. The minimum-lag-threshold can be interpreted as the prediction horizon of the model. We see that the general structure of the observed CO anomalies is preserved for minimum lags under 25 weeks (about half a year).

521 ing data, and test it on the left out year. The average RMSE is then taken for each dif-
 522 ferent training and testing set pair and plotted as a function of minimum-lag-threshold.
 523 We again see that performance falls off, although gradually.

524 We think that the gradual nature of the decline in model performance is a result
 525 of the climate indices exhibiting high auto-correlation (not shown). Since many of the
 526 short lags are highly correlated to longer lags of the same index, we think that these longer
 527 lags are able to explain much of the same CO variability when the shorter lags are ex-
 528 cluded. This is again promising, as it means that predictions can be made decently far
 529 in advance (on the order of a half year) without dramatically compromising performance.

530 To further visualize model performance at increasingly large minimum-lag-thresholds,
 531 we consider predictions for the 2015 CO event in the MSEA region. Figure 9 shows pre-
 532 dictions from the models corresponding to the minimum-lag-thresholds from Figure 8.
 533 The predictions largely capture the structure of the CO observations for minimum-lag-
 534 thresholds below 25 weeks (about six months). After this point, the predictions begin
 535 to flatten out (i.e., not capture the extremes in the response) and the predicted spike starts
 536 earlier in the year (i.e., in early September instead of early October). This result largely
 537 agrees with Shawki et al. (2017), who found that a drought metric could be reasonably
 538 predicted 180 days (about 25 weeks) in advance. However, unlike Shawki et al. (2017),
 539 our predictions rely solely on past climate mode index anomalies, rather than forecasts
 540 from a global climate model.

541 These results indicate that our models can be useful for predicting the structure
 542 of the CO anomalies up to six months in advance for MSEA. However, if a very high level

543 of fidelity is required on a weekly timescale, then restricting predictions to less than a
544 three-month lead time is advised.

545 **7 Summary**

546 We build on previous work aimed at explaining the relationship between climate
547 and atmospheric CO variability. Atmospheric CO is a useful proxy for fire intensity, as
548 fires are the main source of CO variability in the Southern Hemisphere and CO is remotely
549 sensed on a global scale.

550 Our proposed regularization framework highlights a variety of optimally perform-
551 ing models at decreasing complexities, isolating the most important indices and lag val-
552 ues as the models become more parsimonious. Notably, for the MSEA region, we iden-
553 tify the Niño 3.4 index lagged at four weeks as a primary driver of atmospheric CO. Other
554 important climate indices are the DMI and OLR (as a proxy for the MJO). We further
555 identify that Niño 3.4 interactions with the OLR and DMI are significant predictors, sug-
556 gesting that the effect of these indices is amplified when they are in phase. Note that
557 these results largely agree and expand upon those presented in Buchholz et al. (2018).
558 Finally, we show that including multiple lags of the DMI is important for explaining CO
559 variability in MSEA.

560 We also perform a resampling-based sensitivity analysis to quantify the robustness
561 of the model fit to all of the data. We find that the models forced to retain the covari-
562 ates from the model fit to all of the data perform as good or better than the models al-
563 lowed to completely change based on the training set. This provides justification for us-
564 ing the models from Figure 4 as the representative models for the MSEA region. Ad-
565 ditionally, we determine which covariates are most likely to remain in model when trained
566 on slightly different data, finding that the terms in the most parsimonious model from
567 Figure 4 are also the most robust. This justifies assigning scientific weight to the selec-
568 tion of these terms, as it suggests that they are capturing a physically-based relation-
569 ship and are not simply artifacts of the specific training set used.

570 We show that our model for the MSEA region can explain around 70% of the vari-
571 ability in the weekly CO anomalies solely using climate indices as predictor variables.
572 We further use model predictions to highlight the importance of the OLR (as a proxy
573 for the MJO) in overall model performance and in explaining the most extreme CO anoma-
574 lies. Similarly, we show that month-averaged predictions from a model trained on week-
575 averaged data outperform predictions from a model trained on month-averaged data. This
576 suggests that there is meaningful signal in the week-averaged data and justifies its use
577 over month-averaged data. Note that the predictions from these models are an improve-
578 ment over those in Buchholz et al. (2018), as they explain 87% of the variability in month-
579 averaged CO observations compared to 75%.

580 Finally, we perform a minimum-lag-threshold study to assess the predictive capa-
581 bilities of our models at longer lead times. We find that models for the MSEA region are
582 still able to explain around 65% of the weekly atmospheric CO variability when forced
583 to only use lags greater than 35 weeks. This indicates that predictions can be made rel-
584 atively far in advance without losing the overall structure and general amplitude of the
585 CO anomalies. If these models are to provide advanced warning of fire season intensity,
586 then longer lead times are beneficial because they extend the time available to prepare.

Acknowledgments

The NCAR MOPITT project is supported by the National Aeronautics and Space Administration (NASA) Earth Observing System (EOS) Program. The MOPITT team also acknowledges support from the Canadian Space Agency (CSA), the Natural Sciences and Engineering Research Council (NSERC) and Environment Canada, and the contributions of COMDEV and ABB BOMEM. The National Center for Atmospheric Research (NCAR) is sponsored by the National Science Foundation.

Open Research

MOPITT carbon monoxide data are publicly available through NASA. See DOI: 10.5067/TERRA/MOPITT/MOP02J.L2.008. Climate index data are produced and maintained by NOAA. See: <https://stateoftheocean.osmc.noaa.gov> and <http://www.cpc.ncep.noaa.gov>. Only a subset of the MOPITT V8 Level 2 carbon monoxide data are used in this work. Filtered carbon monoxide and climate mode index data can be found on Github, along with R code to implement the model fitting framework proposed in this work. See: <https://github.com/wsdaniels/COmodeling>.

References

- Alencar, A., Asner, G. P., Knapp, D., & Zarin, D. (2011). Temporal variability of forest fires in eastern Amazonia. *Ecological Applications*, *21*(7), 2397–2412. doi: 10.1890/10-1168.1
- Andela, N., & van der Werf, G. R. (2014). Recent trends in African fires driven by cropland expansion and El Niño to la Niña transition. *Nature Climate Change*, *4*(9), 791–795. doi: 10.1038/nclimate2313
- Andreoli, R. V., & Kayano, M. T. (2006). Tropical Pacific and South Atlantic effects on rainfall variability over Northeast Brazil. *International Journal of Climatology*, *26*(13), 1895–1912. doi: 10.1002/joc.1341
- Bamston, A. G., Chelliah, M., & Goldenberg, S. B. (1997). Documentation of a highly ENSO-related sst region in the equatorial pacific: Research note. *Atmosphere - Ocean*, *35*(3), 367–383. doi: 10.1080/07055900.1997.9649597
- Birch, C. E., Webster, S., Peatman, S. C., Parker, D. J., Matthews, A. J., Li, Y., & Hassim, M. E. E. (2016). Scale interactions between the MJO and the Western Maritime Continent. *Journal of Climate*, *29*, 2471–2492. doi: 10.1175/JCLI-D-15-0557.1
- Bloom, A. A., Worden, J., Jiang, Z., Worden, H., Kurosu, T., Frankenberg, C., & Schimel, D. (2015). Remote-sensing constraints on South America fire traits by Bayesian fusion of atmospheric and surface data. *Geophysical Research Letters*, *42*(4), 1268–1274. doi: 10.1002/2014GL062584
- Buchholz, R. R., Hammerling, D., Worden, H. M., Deeter, M. N., Emmons, L. K., Edwards, D. P., & Monks, S. A. (2018). Links between carbon monoxide and climate indices for the Southern Hemisphere and tropical fire regions. *Journal of Geophysical Research: Atmospheres*, *123*(17), 9786–9800. doi: 10.1029/2018JD028438
- Buchholz, R. R., Worden, H. M., Park, M., Francis, G., Deeter, M. N., Edwards, D. P., . . . Kulawik, S. S. (2021). Air pollution trends measured from Terra: CO and AOD over industrial, fire-prone, and background regions. *Remote Sensing of Environment*, *256*, 112275. doi: <https://doi.org/10.1016/j.rse.2020.112275>
- Ceccato, P., Nengah Surati Jaya, I., Qian, J. H., Tippet, M. K., Robertson, A. W., & Someshwar, S. (2010). *Early warning and response to fires in Kalimantan, Indonesia* (Tech. Rep.). International Research Institute for Climate and Society.

- 637 Chen, Y., Morton, D. C., Andela, N., Giglio, L., & Randerson, J. T. (2016). How
638 much global burned area can be forecast on seasonal time scales using sea
639 surface temperatures? *Environmental Research Letters*, *11*(4), 45001. doi:
640 10.1088/1748-9326/11/4/045001
- 641 Chen, Y., Morton, D. C., Andela, N., van der Werf, G. R., Giglio, L., & Rander-
642 son, J. T. (2017). A pan-tropical cascade of fire driven by El Niño/Southern
643 Oscillation. *Nature Climate Change* *2017 7:12*, *7*, 906-911. doi: 10.1038/
644 s41558-017-0014-8
- 645 Cleverly, J., Eamus, D., Luo, Q., Coupe, N. R., Kljun, N., Ma, X., . . . Huete, A.
646 (2016). The importance of interacting climate modes on Australia’s contri-
647 bution to global carbon cycle extremes. *Scientific Reports*, *6*(1), 1–10. doi:
648 10.1038/srep23113
- 649 Deeter, M. N., Edwards, D. P., Francis, G. L., Gille, J. C., Mao, D., Martínez-
650 Alonso, S., . . . Andreae, M. O. (2019). Radiance-based retrieval bias mit-
651 igation for the MOPITT instrument: The version 8 product. *Atmospheric*
652 *Measurement Techniques*, *12*(8), 4561–4580. doi: 10.5194/amt-12-4561-2019
- 653 Deeter, M. N., Edwards, D. P., Gille, J. C., & Drummond, J. R. (2007). Sensitivity
654 of MOPITT observations to carbon monoxide in the lower troposphere. *Jour-
655 nal of Geophysical Research*, *112*(D24), D24306. doi: 10.1029/2007JD008929
- 656 Deeter, M. N., Martínez-Alonso, S., Edwards, D. P., Emmons, L. K., Gille, J. C.,
657 Worden, H. M., . . . Wofsy, S. C. (2014). The MOPITT Version 6 product: Al-
658 gorithm enhancements and validation. *Atmospheric Measurement Techniques*,
659 *7*(11), 3623–3632. doi: 10.5194/amt-7-3623-2014
- 660 Drummond, J. R., Zou, J., Nichitiu, F., Kar, J., Deschambaut, R., & Hack-
661 ett, J. (2010). A review of 9-year performance and operation of the
662 MOPITT instrument. *Advances in Space Research*, *45*, 760-774. doi:
663 10.1016/J.ASR.2009.11.019
- 664 Edwards, D. P., Emmons, L. K., Gille, J. C., Chu, A., Attié, J.-L., Giglio, L., . . .
665 Drummond, J. R. (2006). Satellite-observed pollution from Southern Hemi-
666 sphere biomass burning. *Journal of Geophysical Research*, *111*(D14), D14312.
667 doi: 10.1029/2005JD006655
- 668 Edwards, D. P., Pétron, G., Novelli, P. C., Emmons, L. K., Gille, J. C., & Drum-
669 mond, J. R. (2006). Southern Hemisphere carbon monoxide interan-
670 nual variability observed by Terra/Measurement of Pollution in the Tropo-
671 sphere (MOPITT). *Journal of Geophysical Research*, *111*, D16303. doi:
672 10.1029/2006JD007079
- 673 Enfield, D. B., Mestas-Nuñez, A. M., Mayer, D. A., & Cid-Serrano, L. (1999). How
674 ubiquitous is the dipole relationship in tropical Atlantic sea surface tempera-
675 tures? *Journal of Geophysical Research: Oceans*, *104*(C4), 7841–7848. doi:
676 10.1029/1998jc900109
- 677 Fonseca, M. G., Anderson, L. O., Arai, E., Shimabukuro, Y. E., Xaud, H. A. M.,
678 Xaud, M. R., . . . Aragão, L. E. O. C. (2017). Climatic and anthropogenic
679 drivers of northern Amazon fires during the 2015–2016 El Niño event. *Ecologi-
680 cal Applications*, *27*, 2514-2527. doi: 10.1002/EAP.1628
- 681 Fuller, D. O., & Murphy, K. (2006). The ENSO-fire dynamic in insular Southeast
682 Asia. *Climatic Change*, *74*(4), 435–455. doi: 10.1007/s10584-006-0432-5
- 683 Giglio, L., Boschetti, L., Roy, D. P., Humber, M. L., & Justice, C. O. (2018). The
684 Collection 6 MODIS burned area mapping algorithm and product. *Remote*
685 *Sensing of Environment*, *217*, 72–85. doi: 10.1016/j.rse.2018.08.005
- 686 Giglio, L., Schroeder, W., & Justice, C. O. (2016). The collection 6 MODIS active
687 fire detection algorithm and fire products. *Remote Sensing of Environment*,
688 *178*, 31–41. doi: 10.1016/j.rse.2016.02.054
- 689 Hao, N., Feng, Y., & Zhang, H. H. (2018). Model selection for high-dimensional
690 quadratic regression via regularization. *Journal of the American Statistical As-
691 sociation*, *113*(522), 615–625. doi: 10.1080/01621459.2016.1264956

- 692 Holloway, T., Levy, H., & Kasibhatla, P. (2000). Global distribution of carbon
693 monoxide. *Journal of Geophysical Research: Atmospheres*, *105*(D10), 12123–
694 12147. doi: 10.1029/1999JD901173
- 695 Kalnay, E., Kanamitsu, M., Kistler, R., Collins, W., Deaven, D., Gandin, L.,
696 ... Joseph, D. (1996). The NCEP/NCAR 40-year reanalysis project.
697 *Bulletin of the American Meteorological Society*, *77*(3), 437 - 472. doi:
698 10.1175/1520-0477(1996)077<0437:TNYRP>2.0.CO;2
- 699 Kistler, R., Kalnay, E., Collins, W., Saha, S., White, G., Woollen, J., ... Fiorino,
700 M. (2001). The NCEP–NCAR 50-year reanalysis: Monthly means CD-ROM
701 and documentation. *Bulletin of the American Meteorological Society*, *82*(2),
702 247–268.
- 703 Madden, R. A., & Julian, P. R. (1972). Description of global-scale circula-
704 tion cells in the tropics with a 40–50 day period. *Journal of Atmospheric*
705 *Sciences*, *29*(6), 1109 - 1123. doi: 10.1175/1520-0469(1972)029<1109:
706 DOGSCC>2.0.CO;2
- 707 Madden, R. A., & Julian, P. R. (1994). Observations of the 40–50-day tropical os-
708 cillation—a review. *Monthly Weather Review*, *122*(5), 814 - 837. doi: 10.1175/
709 1520-0493(1994)122<0814:OOTDTP>2.0.CO;2
- 710 Mason, S. A., Hamlington, P. E., Hamlington, B. D., Jolly, W. M., & Hoffman,
711 C. M. (2017). Effects of climate oscillations on wildland fire potential in the
712 continental United States. *Geophysical Research Letters*, *44*, 7002-7010. doi:
713 10.1002/2017GL074111
- 714 N'Datchoh, E. T., Konaré, A., Diedhiou, A., Diawara, A., Quansah, E., & Assamoi,
715 P. (2015). Effects of climate variability on savannah fire regimes in West
716 Africa. *Earth System Dynamics*, *6*, 161-174. doi: 10.5194/ESD-6-161-2015
- 717 Neelin, J. D., Battisti, D. S., Hirst, A. C., Jin, F. F., Wakata, Y., Yamagata, T., &
718 Zebiak, S. E. (1998). ENSO theory. *Journal of Geophysical Research: Oceans*,
719 *103*(C7), 14261–14290. doi: 10.1029/97jc03424
- 720 Nelder, J. A. (1977). A reformulation of linear models. *Journal of the Royal Statisti-*
721 *cal Society. Series A (General)*, *140*(1), 48. doi: 10.2307/2344517
- 722 NOAA CPC. (2021). *Climate prediction center - teleconnections: Antarctic oscilla-*
723 *tion*. [https://www.cpc.ncep.noaa.gov/products/precip/CWlink/daily_ao](https://www.cpc.ncep.noaa.gov/products/precip/CWlink/daily_ao_index/ao/ao.shtml)
724 [_index/ao/ao.shtml](https://www.cpc.ncep.noaa.gov/products/precip/CWlink/daily_ao_index/ao/ao.shtml).
- 725 NOAA OOPC. (2021). *Ocean observations panel for climate - state of the ocean cli-*
726 *mate*. <https://stateoftheocean.osmc.noaa.gov/>.
- 727 NOAA PSL. (2021). *Physical sciences laboratory - interpolated olr*. [https://psl](https://psl.noaa.gov/data/gridded/data.interp_OLR.html)
728 [.noaa.gov/data/gridded/data.interp_OLR.html](https://psl.noaa.gov/data/gridded/data.interp_OLR.html).
- 729 Nur'utami, M. N., & Hidayat, R. (2016). Influences of IOD and ENSO to In-
730 donesian rainfall variability: Role of atmosphere-ocean interaction in the
731 Indo-pacific sector. *Procedia Environmental Sciences*, *33*, 196–203. doi:
732 10.1016/j.proenv.2016.03.070
- 733 Reid, J. S., Xian, P., Hyer, E. J., Flatau, M. K., Ramirez, E. M., Turk, F. J., ...
734 Maloney, E. D. (2012). Multi-scale meteorological conceptual analysis of ob-
735 served active fire hotspot activity and smoke optical depth in the Maritime
736 Continent. *Atmospheric Chemistry and Physics*, *12*(4), 2117–2147. doi:
737 10.5194/acp-12-2117-2012
- 738 Saji, N. H., Goswami, B. N., Vinayachandran, P. N., & Yamagata, T. (1999). A
739 dipole mode in the tropical Indian ocean. *Nature*, *401*(6751), 360–363. doi: 10
740 .1038/43854
- 741 Saji, N. H., & Yamagata, T. (2003). Possible impacts of Indian Ocean Dipole mode
742 events on global climate. *Climate Research*, *25*(2), 151–169. doi: 10.3354/
743 cr025151
- 744 Shabbar, A., Skinner, W., & Flannigan, M. D. (2011). Prediction of seasonal forest
745 fire severity in Canada from large-scale climate patterns. *Journal of Applied*
746 *Meteorology and Climatology*, *50*(4), 785–799. doi: 10.1175/2010JAMC2547.1

- 747 Shawki, D., Field, R. D., Tippett, M. K., Saharjo, B. H., Albar, I., Atmoko, D.,
748 & Voulgarakis, A. (2017). Long-lead prediction of the 2015 fire and haze
749 episode in Indonesia. *Geophysical Research Letters*, *44*(19), 9996. doi:
750 10.1002/2017GL073660
- 751 Thompson, D. W. J., & Wallace, J. M. (2000). Annular modes in the extratropi-
752 cal circulation. Part I: Month-to-month variability. *Journal of Climate*, *13*(5),
753 1000 - 1016. doi: 10.1175/1520-0442(2000)013<1000:AMITEC>2.0.CO;2
- 754 Tibshirani, R. (1996). Regression shrinkage and selection via the lasso. *Journal*
755 *of the Royal Statistical Society: Series B (Methodological)*, *58*, 267-288. doi: 10
756 .1111/J.2517-6161.1996.TB02080.X
- 757 Trenberth, K. (2013). *El Nino Southern Oscillation (ENSO)* (Tech. Rep.). National
758 Center for Atmospheric Research (NCAR).
- 759 van der Werf, G. R., Randerson, J. T., Giglio, L., Gobron, N., & Dolman, A. J.
760 (2008). Climate controls on the variability of fires in the tropics and subtrop-
761 ics. *Global Biogeochemical Cycles*, *22*(3). doi: 10.1029/2007GB003122
- 762 Voulgarakis, A., Marlier, M. E., Faluvegi, G., Shindell, D. T., Tsigaridis, K., &
763 Mangeon, S. (2015). Interannual variability of tropospheric trace gases and
764 aerosols: The role of biomass burning emissions. *Journal of Geophysical Re-*
765 *search: Atmospheres*, *120*(14), 7157–7173. doi: 10.1002/2014JD022926
- 766 Wheeler, M. C., & Hendon, H. H. (2004). An all-season real-time multivariate
767 MJO index: Development of an index for monitoring and prediction. *Monthly*
768 *Weather Review*, *132*(8), 1917 - 1932. doi: 10.1175/1520-0493(2004)132<1917:
769 AARMMI>2.0.CO;2
- 770 Wooster, M. J., Perry, G. L., & Zoumas, A. (2012). Fire, drought and El Niño rela-
771 tionships on Borneo (Southeast Asia) in the pre-MODIS era (1980-2000). *Bio-*
772 *geosciences*, *9*(1), 317–340. doi: 10.5194/bg-9-317-2012
- 773 Worden, H. M., Deeter, M. N., Edwards, D. P., Gille, J. C., Drummond, J. R., &
774 Nédélec, P. (2010). Observations of near-surface carbon monoxide from space
775 using mopitt multispectral retrievals. *Journal of Geophysical Research: Atmo-*
776 *spheres*, *115*, 18314. doi: 10.1029/2010JD014242
- 777 Xavier, P., Rahmat, R., Cheong, W. K., & Wallace, E. (2014). Influence of
778 Madden-Julian Oscillation on Southeast Asia rainfall extremes: Observa-
779 tions and predictability. *Geophysical Research Letters*, *41*(12), 4406–4412. doi:
780 10.1002/2014GL060241
- 781 Zhang, C.-H. (2010). Nearly unbiased variable selection under minimax concave
782 penalty. *The Annals of Statistics*, *38*(2), 894–942. doi: 10.1214/09-AOS729